

Non-Trivial Oblique Spin Equilibria of Super-Earths in Multi-planetary Systems

Yubo Su,^{1*} Dong Lai,¹

¹Cornell Center for Astrophysics and Planetary Science, Department of Astronomy,
Cornell University, Ithaca, NY 14853, USA

Many Sun-like stars are observed to host close-in super-Earths (SEs) as part of a multi-planetary system. In such a system, the spin of the SE evolves due to spin-orbit resonances and tidal dissipation. In the absence of tides, the planet’s obliquity can evolve chaotically to large values. However, for close-in SEs, tidal dissipation is significant and suppresses the chaos, instead driving the spin into various steady states. We find that the attracting steady states of the SE’s spin are more numerous than previously thought, due to the discovery of a new class of “mixed-mode” high-obliquity equilibria. These new equilibria arise due to subharmonic responses of the parametrically-driven planetary spin, an unusual phenomenon that arises in nonlinear systems. Many SEs should therefore have significant obliquities, with potentially large impacts on the physical conditions of their surfaces and atmospheres.

Introduction. The obliquity of a planet, the angle between the spin and orbital axes, plays an important role in the atmospheric dynamics, climate, and potential habitability of the planet. For instance, the atmospheric circulation of a planet changes dramatically as the obliquity increases beyond 54° , as the averaged insolation at the poles becomes greater than that at the equator (1, 2). Variations in insolation over long timescales can also affect the habitability of an exoplanet (3, 4). In the Solar System, planetary obliquities range from nearly zero for Mercury and 3.1° for Jupiter, to 23° for Earth and 26.7° for Saturn, to 98° for Uranus. The obliquities of exoplanets are challenging to measure, and so far only loose constraints have been obtained for the obliquities of faraway planetary-mass companions (5, 6). Nevertheless, there are prospects for better constraints on exoplanetary obliquities in the coming years (7–9). Substantial obliquities are of great theoretical interest for their proposed role in explaining peculiar thermal phase curves of transiting planets (10, 11) and various other dynamical puzzles (12–15).

The obliquity of a planet reflects its dynamical history. Some obliquities could be generated in the earliest phase of planet formation, when/if proto-planetary disks are turbulent and twisted (16, 17). Large obliquities are commonly attributed to giant impacts or planet collisions as a result of dynamical instabilities of planetary orbits (18–24). Repeated planet-planet scatterings could also lead to modest obliquities (25, 26). Substantial obliquity excitation can be achieved over long (secular) timescales via spin-orbit resonances, when the spin precession and orbital (nodal) precession frequencies of the planet

become comparable (27–34). Such resonances are likely responsible for the obliquities of the Solar System gas giants and may have also played a role in generating obliquities of ice giants (35). For terrestrial planets, multiple spin-orbit resonances and their overlaps can make the obliquity vary chaotically over a wide range (36–38).

A large fraction (30–90%) of Sun-like stars host close-in super-Earths (SEs), with radii $1–4R_{\oplus}$ and orbital distances $\lesssim 0.5$ AU, mostly in multi-planetary (≥ 3) systems [e.g. (39–44)]. In these systems, the SE orbits are mildly misaligned with mutual inclinations $\sim 2^\circ$ (39, 45, 46), which increase as the number of planets in the system decreases (41, 47). In addition, ~ 30 –40% of the SE systems are accompanied by cold Jupiters [CJs; masses $\gtrsim 0.5M_J$ and semi-major axes $\gtrsim 1$ AU, (48, 49)] with significantly inclined ($\gtrsim 10^\circ$) orbits relative to the SEs (50).

SEs are formed in gaseous protoplanetary disks, and likely have experienced an earlier phase of giant impacts and collisions following the dispersal of disks [e.g. (51–53)]. As a result, the SEs’ initial obliquities are expected to be broadly distributed (23, 24). However, due to the proximity of these planets to their host stars, tidal dissipation can change the planets’ spin rates and orientations substantially within the age of the planetary system. Indeed, the tidal spin-orbit alignment timescale is given by

$$t_{\text{al}} \simeq (30 \text{ Myr}) \left(\frac{Q/2k_2}{10^3} \right) \left(\frac{M_{\star}}{M_{\odot}} \right)^{-3/2} \left(\frac{m}{4m_{\oplus}} \right) \left(\frac{R}{2R_{\oplus}} \right)^{-3} \left(\frac{a}{0.4 \text{ AU}} \right)^{9/2}, \quad (1)$$

where m , R , k_2 , Q , and a are the planet’s mass, radius, tidal Love number, tidal quality factor, and semi-major axis respectively, and M_{\star} is the stellar mass. In a previous paper (15), we have studied the combined effects of spin-orbit resonance and tidal dissipation in a two-planet system (i.e. a SE with a companion), and showed that the planet’s spin can only evolve into two possible long-term equilibria (“Tidal Cassini Equilibria”), one of which can have a significant obliquity. In this paper, we extend our analysis to three-planet systems consisting of either three SEs or two SEs and a CJ. In addition to the equilibria analogous to those of the two-planet case, we discover a novel class of oblique spin equilibria unique to multi-planet systems. Such equilibria can substantially increase the occurrence rate of oblique SEs in these architectures.

Spin Equations of Motion. The unit spin vector $\hat{\mathbf{S}}$ of an oblate planet orbiting a host star precesses around the planet’s unit angular momentum $\hat{\mathbf{L}}$ following the equation

$$\frac{d\hat{\mathbf{S}}}{dt} = \alpha \left(\hat{\mathbf{S}} \cdot \hat{\mathbf{L}} \right) \left(\hat{\mathbf{S}} \times \hat{\mathbf{L}} \right), \quad (2)$$

where the characteristic spin-orbit precession frequency α is given by

$$\begin{aligned} \alpha &= \frac{3GJ_2mR^2M_{\star}}{2a^3C\Omega_s} = \frac{3k_q}{2k} \frac{M_{\star}}{m} \left(\frac{R}{a} \right)^3 \Omega_s \\ &= \frac{1}{150 \text{ yr}} \left(\frac{k_q}{k} \right) \left(\frac{M_{\star}}{M_{\odot}} \right)^{3/2} \left(\frac{m}{2M_{\oplus}} \right)^{-1} \left(\frac{R}{1.2R_{\oplus}} \right)^3 \left(\frac{a}{0.1 \text{ AU}} \right)^{-9/2} \frac{\Omega_s}{n}. \end{aligned} \quad (3)$$

In Eq. (3), Ω_s is the rotation rate of the planet, $C = kmR^2$ is its moment of inertia (with k the normalized moment of inertia), $J_2 = k_q\Omega_s^2(R^3/Gm)$ (with k_q a constant) is its rotation-induced (dimensionless) quadrupole moment, and $n \equiv \sqrt{GM_{\star}/a^3}$ is its mean motion. For a SE, we adopt $k \sim k_q \sim 0.3$ [e.g. (54, 55)].

The orbital axis $\hat{\mathbf{L}}$ also evolves in time, precessing and nutating about the total angular momentum axis of the exoplanetary system, which we denote by $\hat{\mathbf{J}}$. When there are just two planets, this precession is uniform (with rate g and constant inclination angle between $\hat{\mathbf{L}}$ and $\hat{\mathbf{J}}$), and the spin dynamics of the planet is described by the well-studied ‘‘Colombo’s Top’’ system (56–60). The spin equilibria of this system are termed ‘‘Cassini States’’ (CSs), and the number of CSs and their obliquities depend on the ratio $\eta \equiv |g|/\alpha$. In the presence of a tidal spin-orbit alignment torque, up to two equilibria are stable and attracting, as shown in [(15); see also (61–63)]: for $\eta \gg 1$, only CS2 is stable, with $\hat{\mathbf{S}}$ nearly aligned with $\hat{\mathbf{J}}$; for $\eta \lesssim 1$, $\hat{\mathbf{S}}$ can evolve towards two possible states, the ‘‘trivial’’ CS1 with a small spin-orbit misalignment angle θ_{sl} , or the ‘‘resonant’’ CS2 with significant θ_{sl} (which approaches 90° for $\eta \ll 1$).

When the SE is surrounded by multiple companions, the precession of $\hat{\mathbf{L}}$ occurs on multiple characteristic frequencies [see (64)]. In this case, the spin dynamics given by Eq. (2) is complex and can lead to chaotic behavior [e.g. the chaotic obliquity evolution of Mars (36, 37)]. But what is the final equilibrium state of $\hat{\mathbf{S}}$ in the presence of tidal alignment? In this paper, we focus on the case where the SE has two planetary companions. If the mutual inclinations among the three planets are small, then the explicit solution for $\hat{\mathbf{L}}(t)$ can be written as (64)

$$\mathcal{I} \equiv I \exp(i\Omega) = I_{(\text{I})} \exp[ig_{(\text{I})}t + i\phi_{(\text{I})}] + I_{(\text{II})} \exp[ig_{(\text{II})}t + i\phi_{(\text{II})}], \quad (4)$$

$$\hat{\mathbf{L}} = \text{Re}(\mathcal{I}) \hat{\mathbf{X}} + \text{Im}(\mathcal{I}) \hat{\mathbf{Y}} + \sqrt{1 - |\mathcal{I}|^2} \hat{\mathbf{Z}}. \quad (5)$$

Here, I is the inclination of $\hat{\mathbf{L}}$ relative to $\hat{\mathbf{J}}$, \mathcal{I} is the complex inclination, the quantities $I_{(\text{I,II})}$, $g_{(\text{I,II})}$ and $\phi_{(\text{I,II})}$ are the amplitudes, frequencies, and phase offsets of the two inclination modes, indexed by (I) and (II), and the Cartesian coordinate system XYZ is defined such that $\hat{\mathbf{J}} = \hat{\mathbf{Z}}$. Without loss of generality, we denote mode I as the dominant mode, with $I_{(\text{I})} \geq I_{(\text{II})}$. For simplicity, we fix $\phi_{(\text{I})} = \phi_{(\text{II})} = 0$.

Steady States Under Tidal Alignment Torque. Since SEs are close to their host stars, tidal torques tend to drive $\hat{\mathbf{S}}$ towards alignment with $\hat{\mathbf{L}}$ and Ω_s towards synchronization with the mean motion (see Eq. 1). As the evolution of Ω_s also changes α (Eq. 3) and the underlying phase-space structure, we first consider the dynamics when ignoring the spin magnitude evolution. In this case, the planet’s spin orientation experiences an alignment torque, which we describe by

$$\left(\frac{d\hat{\mathbf{S}}}{dt} \right)_{\text{al}} = \frac{1}{t_{\text{al}}} \hat{\mathbf{S}} \times (\hat{\mathbf{L}} \times \hat{\mathbf{S}}), \quad (6)$$

where t_{al} is given by Eq. (1). Note that t_{al} is significantly longer than all precession timescales in the system.

With two precessional modes for $\hat{\mathbf{L}}(t)$, we expect that the tidally stable spin equilibria (steady states) correspond to the stable, attracting CSs for each mode, when they exist. In other words, if we denote the CS2 corresponding to mode I by CS2(I), then we expect that the tidally stable equilibria are among the four CSs: CS1(I) (if it exists), CS2(I), CS1(II) (if it exists), and CS2(II). The corresponding CS obliquities $\theta_{\text{sl}} \equiv \cos^{-1}(\hat{\mathbf{S}} \cdot \hat{\mathbf{L}})$ are given by

$$\alpha \cos \theta_{\text{sl}} = -g_{(\text{I,II})} (\cos I_{(\text{I,II})} + \sin I_{(\text{I,II})} \cot \theta_{\text{sl}} \cos \phi_{\text{sl}}), \quad (7)$$

where the azimuthal angle ϕ_{sl} of $\hat{\mathbf{S}}$ around $\hat{\mathbf{L}}$ is $\phi_{\text{sl}} = 0$ (corresponding to $\hat{\mathbf{S}}$ and $\hat{\mathbf{J}}$ being coplanar but on opposite sides of $\hat{\mathbf{L}}$) for CS1 and $\phi_{\text{sl}} = \pi$ for CS2 [note that because of the tidal alignment torque, the actual ϕ_{sl} value is slightly shifted from 0 or π ; see (15)].

To confront this expectation, we integrate Eqs. (2), (5), and (6) numerically starting from various spin orientations. Figure 1 shows two evolutionary trajectories for a system with $I_{(\text{I})} = 10^\circ$, $I_{(\text{II})} = 1^\circ$, $|g_{(\text{I})}| = 0.1\alpha$, and $|g_{(\text{II})}| = 0.01\alpha$. Such a system can be realized, for instance, by three SEs with masses M_\oplus , $3M_\oplus$, and $3M_\oplus$ and semi-major axes 0.1 AU, 0.15 AU, and 0.4 AU (see the left panels of Fig. A.1 in the Appendix¹). We see that the initially retrograde spin is eventually captured into a steady state centered around CS1 or CS2 of the dominant mode (i.e. mode I), with ϕ_{sl} librating around 0 or π , respectively. The small oscillation of the final θ_{sl} is the result of perturbations from mode II.

In addition to CS1(I) and CS2(I), we find that the spin can also settle down into other equilibria (steady states) with different librating angles. In general, we define the resonant phase angle

$$\phi_{\text{res}} \equiv \phi_{\text{sl}} - g_{\text{res}}t. \quad (8)$$

The examples shown in Fig. 1 correspond to $g_{\text{res}} = 0$. In Fig. 2, we show three evolutionary trajectories (with three different initial spin orientations) of a system with the same parameters as in Fig. 1 but with $g_{(\text{II})} = -\alpha$. Such a system can be realized, for instance, by two warm SEs orbited by a cold Jupiter (see the right panels of Fig. A.3 in the Appendix where a_3 is small). Among these three examples, the first is captured into a resonance with $g_{\text{res}} = 0$ [i.e. CS2(I)], the second is captured into a resonance with $g_{\text{res}} = \Delta g \equiv g_{(\text{II})} - g_{(\text{I})}$, and the third is captured into a resonance with $g_{\text{res}} = \Delta g/2$.

To explore the regimes under which various resonances are important, we numerically determine [by integrating Eqs. (2), (5), and (6)] the final spin equilibria (steady states) for systems with different mode parameters ($I_{(\text{I})}$, $I_{(\text{II})}$, $g_{(\text{I})}$, and $g_{(\text{II})}$), starting from all possible initial spin orientations. Fig. 3 shows some examples of such a calculation for $I_{(\text{I})} = 10^\circ$, $I_{(\text{II})} = 1^\circ$, $g_{(\text{I})} = -0.1\alpha$ (the same as in Figs. 1–2), but with the four different values of $g_{(\text{II})} = \{0.1, 2.5, 3.5, 10\} \times g_{(\text{I})}$. We identify three qualitatively different regimes:

- When $|g_{(\text{II})}| \ll |g_{(\text{I})}|$ (top-left panel of Fig. 3), mode II serves as a slow, small-amplitude perturbation to the dominant mode I, and the spin evolution is very similar to that studied in Ref. (15): prograde initial conditions (ICs) outside of the mode-I resonance evolve towards CS2(I), ICs inside the resonance evolve to CS2(I), and retrograde ICs outside of the mode-I resonance reach one of the two probabilistically.
- When $|g_{(\text{II})}| \sim |g_{(\text{I})}|$ (see the top-right and bottom-left panels of Fig. 3), the resonances corresponding to the two modes overlap, chaotic obliquity evolution occurs [see (36, 37)], and we expect that CS2(I) becomes less stable². Indeed we see that in this regime, fewer ICs evolve into the high-obliquity CS2(I) equilibrium of the dominant mode I, and most ICs lead to the low-obliquity CS1(I).

¹Note that the mode amplitudes $I_{(\text{I})}$ and $I_{(\text{II})}$ in Fig. A.1 are closer in magnitude than the case we consider here. We exaggerate the inclination hierarchy for a more intuitive physical picture, and explore the case where the modes are of comparable amplitudes later in the paper and in the Appendix.

²An more precise resonance overlap condition can be obtained by comparing the separatrix widths, as the mode-II resonance is much narrower even when $g_{(\text{I})} = g_{(\text{II})}$. Such a condition would require $g_{(\text{I})} \sin I_{(\text{I})} \sim g_{(\text{II})} \sin I_{(\text{II})}$. Thus, the onset of chaos due to resonance overlap occurs somewhere in the range $I_{(\text{II})}/I_{(\text{I})} \lesssim g_{(\text{II})}/g_{(\text{I})} \lesssim 1$.

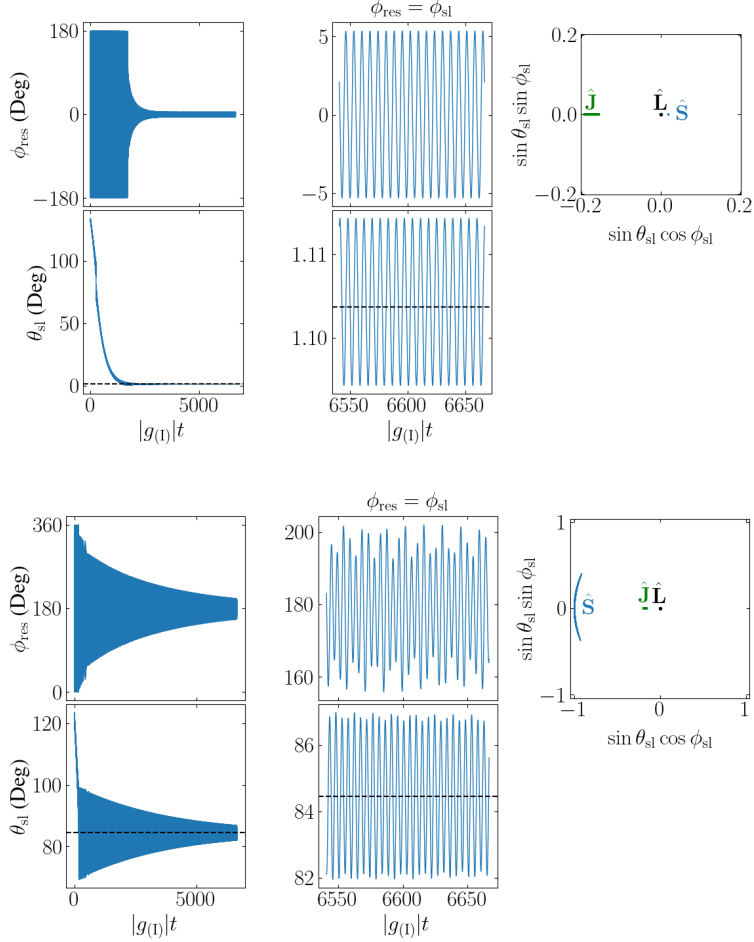


Figure 1: Two evolutionary trajectories of $\hat{\mathbf{S}}$ showing capture into mode I resonances (CSs). In both cases, the mode parameters describing the evolution of $\hat{\mathbf{L}}$ (see Eq. 5) are $I_{(\text{I})} = 10^\circ$, $I_{(\text{II})} = 1^\circ$, $g_{(\text{I})} = -0.1\alpha$, and $g_{(\text{II})} = 0.1g_{(\text{I})}$, while the initial spin orientations differ. In the top group of plots showing capture into CS1(I) [i.e. Cassini State 1 of mode I], the left four panels show the evolution of the spin obliquity θ_{sl} and the resonant phase angle ϕ_{res} ; in this case, ϕ_{res} equals ϕ_{sl} , the azimuthal angle of $\hat{\mathbf{S}}$ around $\hat{\mathbf{L}}$, defined so that $\phi_{\text{sl}} = 0$ corresponds to $\hat{\mathbf{S}}$ and $\hat{\mathbf{J}}$ being coplanar with $\hat{\mathbf{L}}$ but on opposite sides of $\hat{\mathbf{L}}$. The horizontal black dashed line shows the theoretically predicted obliquity of CS1(I), given by Eq. (7). The right panel shows the final steady-state spin axis projected onto the orbital plane (perpendicular to $\hat{\mathbf{L}}$). In these coordinates, $\hat{\mathbf{L}}$ (black dot) is stationary, while $\hat{\mathbf{J}}$ (green line) librates with a fixed orientation, and $\hat{\mathbf{S}}$ is shown in blue. The bottom group of panels shows the same but for capture into the CS2(I) resonance.

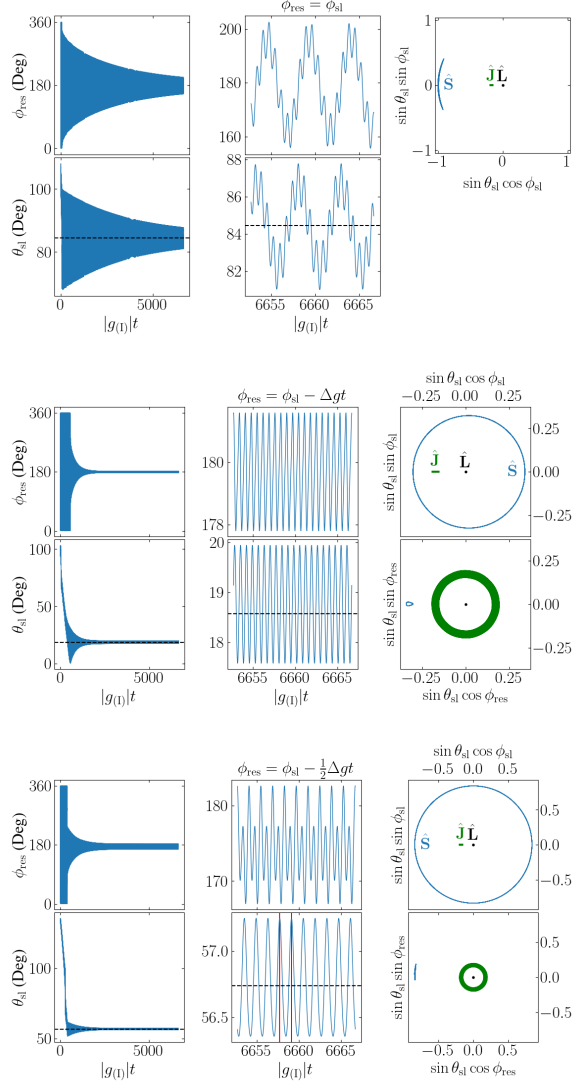


Figure 2: Three evolutionary trajectories for a system with the same parameters as in Fig. 1, except for $g_{(II)} = -\alpha = 10g_{(I)}$. The three examples correspond to capture into CS2(I) (with $\phi_{\text{res}} = \phi_{\text{sl}}$), a resonance with $\phi_{\text{res}} = \phi_{\text{sl}} - \Delta gt$ [corresponding to CS2(II)], and a “mixed mode” resonance with $\phi_{\text{res}} = \phi_{\text{sl}} - \Delta gt/2$, where $\Delta g = g_{(II)} - g_{(I)}$. In the bottom two groups of plots, ϕ_{sl} is not the resonant angle, so the spin axis encircles $\hat{\mathbf{L}}$ in the top-right plots. For these two cases, we also display in the bottom-right panels the projection of the steady-state spin axis onto the $\hat{\mathbf{L}}$ plane but with ϕ_{res} as the azimuthal angle. In these two panels, $\hat{\mathbf{J}}$ encircles $\hat{\mathbf{L}}$ (as shown by the green ring), but the spin can be seen not to encircle $\hat{\mathbf{L}}$, indicating that ϕ_{res} is indeed librating. Finally, for the mixed-mode example (bottom group), the vertical red lines in the bottom-middle panel are separated by $2\pi/|g_{\text{res}}| = 4\pi/|\Delta g|$, denoting the period of oscillation in θ_{sl} .

- When $|g_{(\text{II})}| \gg |g_{(\text{I})}|$ (see the bottom-right panel of Fig. 3), the separatrix for mode II does not exist, we see that all ICs inside the separatrix of mode I again converge successfully to CS2(I), and CS2(II) becomes the preferred low-obliquity equilibrium. Additionally, a narrow band of ICs with $\cos \theta_{\text{sl},0} \sim 0.6$ and some other scattered ICs with $\cos \theta_{\text{sl},0} \lesssim 0.6$ evolve to the mixed-mode equilibrium with $g_{\text{res}} = \Delta g/2$, which has $\theta_{\text{eq}} \approx 60^\circ$. A second mixed-mode resonance with $g_{\text{res}} = \Delta g/3$ is also observed (with $\theta_{\text{eq}} \approx 67^\circ$) for a sparse set of ICs.

Towards a better understanding of how systems are captured into these mixed-mode equilibria, we numerically calculate the “basin of attraction” by repeating the procedure for producing Fig. 3 but instead use a fine grid of ICs with $\theta_{\text{sl},0}$ near the average obliquity of the equilibrium. This results in a “zoomed-in” version of the bottom-right panel of in Fig. 3 and doubles as a numerical stability analysis of the equilibrium. Figure 4 shows the result of this procedure applied to the $g_{\text{res}} = \Delta g/2$ resonance, where we have zoomed in to $\theta_{\text{sl},0}$ near the $\theta_{\text{eq}} \approx 60^\circ$ associated with the resonance. We see that the resonance is reached consistently from some well-defined regions in the $(\theta_{\text{sl}}, \dot{\phi}_{\text{sl}})$ space.

Figure 5 summarizes the equilibrium obliquities θ_{eq} of various resonances achieved for the system depicted in the bottom-right panel of Fig. 3. For a trajectory that reaches a particular equilibrium, we compute $\theta_{\text{eq}} = \langle \theta_{\text{sl}} \rangle$ by averaging over the last $100/\max(|g_{(\text{I})}|, |\Delta g|)$ of the integration. We obtain the corresponding “resonance” frequency by $g_{\text{res}} \simeq \langle \dot{\phi}_{\text{sl}} \rangle$. In the Appendix, we show that the relation between θ_{eq} and g_{res} can be described analytically by

$$\alpha \cos \theta_{\text{eq}} \simeq -g_{(\text{I})} \cos I_{(\text{I})} - g_{\text{res}}. \quad (9)$$

The four systems shown in Fig. 3 demonstrate that the characteristic spin evolution depends strongly on the ratio $g_{(\text{II})}/g_{(\text{I})}$. To understand the transition between these different regimes, we vary $g_{(\text{II})}$ over a wide range of values (while keeping the other parameters the same as in Fig. 3). For each $g_{(\text{II})}$, we numerically determine the steady-state (equilibrium) obliquities and compute the probability of reaching each equilibrium by evolving 3000 initial spin orientations drawn randomly from an isotropic distribution. Figure 6 shows the result. Two trends can be seen: the probability of long-lived capture into the CS2(I) resonance decreases as $|g_{(\text{II})}|$ is increased from $|g_{(\text{II})}| \ll |g_{(\text{I})}|$ to $|g_{(\text{II})}| \sim |g_{(\text{I})}|$, and mixed-mode resonances become significant, though non-dominant, outcomes for $|g_{(\text{II})}| \gg |g_{(\text{I})}|$.

Having discussed how the spin evolution changes when $g_{(\text{II})}$ is varied, we now explore the effect of different values of $I_{(\text{II})}$. In Fig. 7, we display the final outcomes as a function of the initial spin orientation for the same $g_{(\text{II})}$ values as in Fig. 3, but for $I_{(\text{II})} = 3^\circ$. Comparing the bottom-left panels of Figs. 3 and 7 (with $g_{(\text{II})} = 3.5g_{(\text{I})}$), we find that the favored low-obliquity CS changes from CS1(I) to CS1(II) when using $I_{(\text{II})} = 3^\circ$. In both cases, CS2(I) is destabilized such that most initial conditions converge to the low-obliquity CS, either CS1(I) or CS1(II). In the bottom-right panel, we find that many initial conditions converge to other mixed modes than the $g_{\text{res}} = \Delta g/2$ mode. The values of g_{res} observed for the system are shown in Fig. 8, where we find that many low-order rational multiples of $g_{\text{res}}/\Delta g$ are obtained. While the amplitude of oscillation in the final θ_{sl} is substantial (and larger than in Fig. 5), we find that the predictions of Appendix A.2 are consistent with the range of oscillation of θ_{sl} . In Fig. 9, we summarize the outcomes of spin evolution as a function of $g_{(\text{II})}/g_{(\text{I})}$ for $I_{(\text{II})} = 3^\circ$. We identify the same two qualitative trends as seen in Fig. 6: the instability of CS2(I) when $g_{(\text{II})} \sim g_{(\text{I})}$ and the appearance of mixed modes when $|g_{(\text{II})}| \gg |g_{(\text{I})}|$.

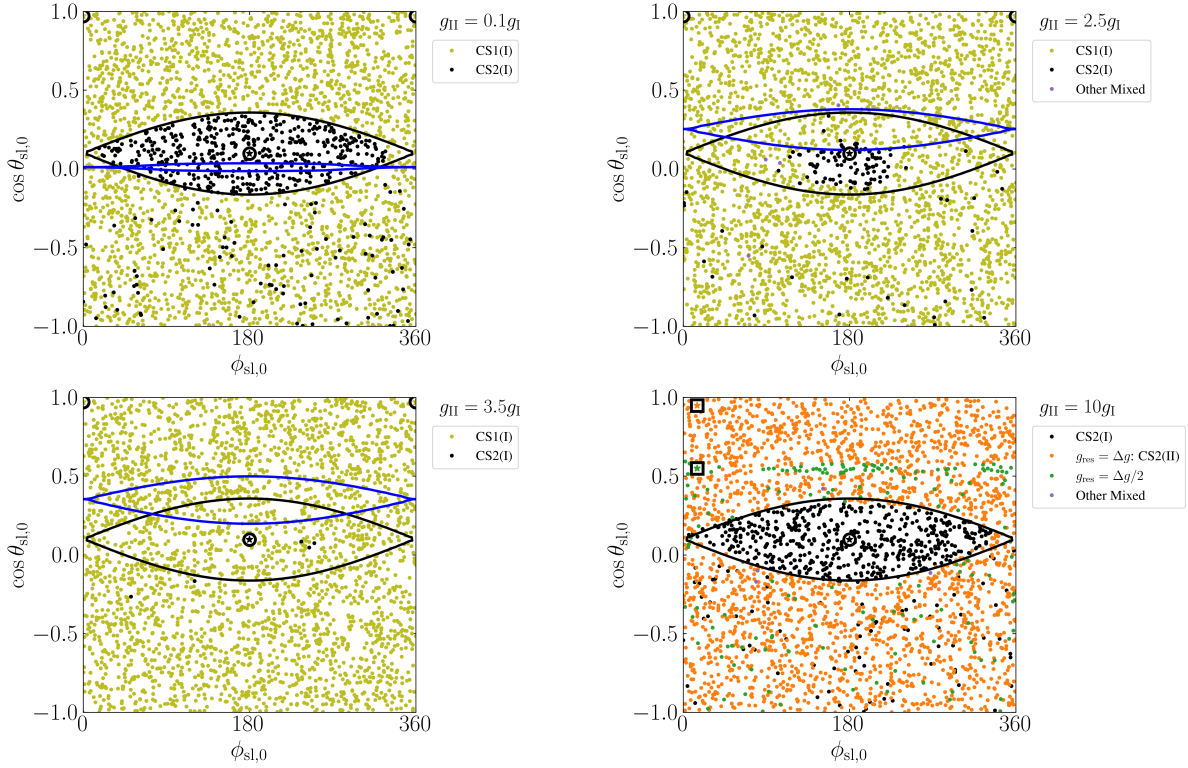


Figure 3: Asymptotic outcomes of spin evolution driven by tidal alignment torque for different initial spin orientations (described by $\theta_{sl,0}$ and $\phi_{sl,0}$) for a system with $I_{(I)} = 10^\circ$, $I_{(II)} = 1^\circ$, $\alpha = 10 |g_{(I)}|$, and $g_{(II)} = \{0.1, 2.5, 3.5, 10\} \times g_{(I)}$ in the top-left, top-right, bottom-left, and bottom-right panels respectively (as labeled). Each dot represents an initial spin orientation, and the coloring of the dot indicates which Cassini State (CS) and which mode (legend) the system evolves into. The obliquity and ϕ_{sl} values of the mode-I CSs are labeled as the circled stars, with the same colors as in the legend. The obliquities of the other equilibria are labeled as the boxed stars at the left edges of the right-bottom panel, with the same colors as in the legend; a small, arbitrary offset in ϕ_{sl} is added to reflect the fact that these equilibria do not have fixed ϕ_{sl} values. The separatrices for the mode I and mode II resonances are given in the black and blue lines respectively.

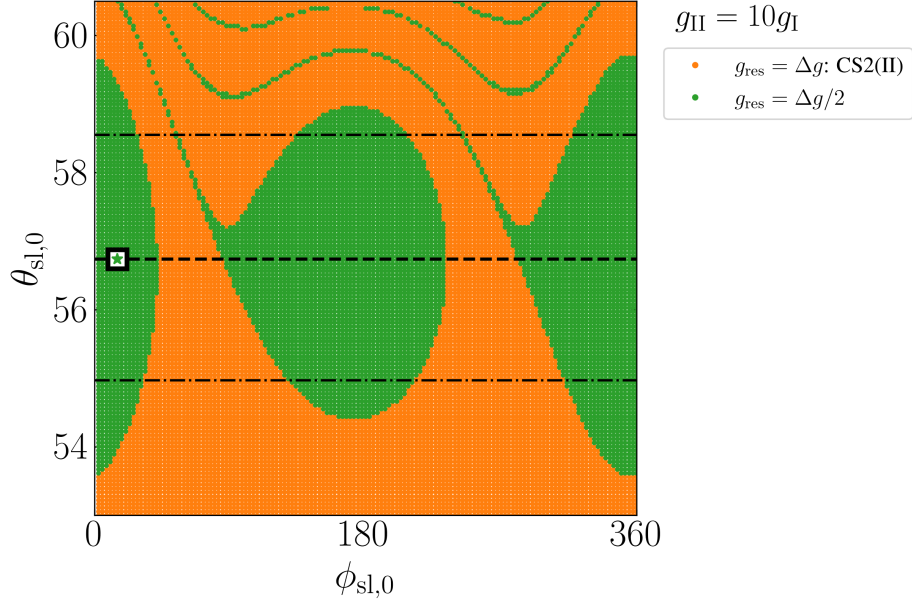


Figure 4: Same as the bottom right panel of Fig. 3 but zoomed-in to a narrow range of initial obliquities near $\theta_{eq} \approx 57^\circ$ (horizontal dashed line) for the $g_{res} = \Delta g/2$ mixed mode equilibrium as predicted by Eq. (9). The horizontal dash-dotted lines indicate the amplitude of oscillation of the mode (see Fig. 2). It is clear that there are two basins of attraction for this mixed-mode resonance near $\phi_{sl,0} = 0$ and $\phi_{sl,0} = 180^\circ$.

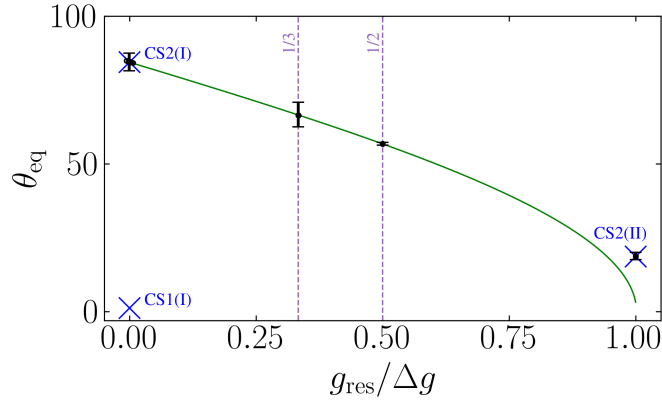


Figure 5: “Equilibrium” obliquity as a function of the resonant frequency (Eq. 8) for a system with $I_{(I)} = 10^\circ$, $I_{(II)} = 1^\circ$, $\alpha = 10 |g_{(I)}|$, and $g_{(II)} = 10g_{(I)}$ (corresponding to the bottom-right panel of Fig. 3). The green line is the analytical result given by Eq. (9). The error bars denote the amplitude of oscillation of θ_{sl} when the spin has reached a steady state (e.g. Figs. 1–2). The blue crosses denote the CSs for the two inclination modes.

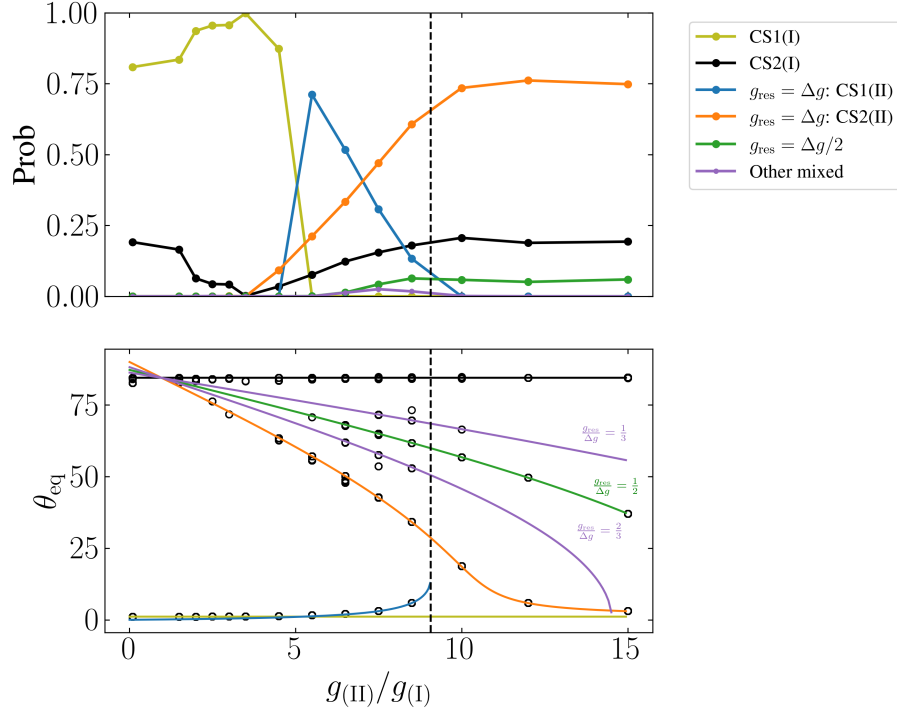


Figure 6: Final outcomes of spin evolution under tidal alignment torque for a 3-planet system with inclination mode parameters $I_{(I)} = 10^\circ$, $I_{(II)} = 1^\circ$, $\alpha = 10 |g_{(I)}|$ (same as Figs. 1–5) and varying $g_{(II)}/g_{(I)}$. The top panel shows the probability of each of the possible steady-state outcomes for 3000 initial spin orientations sampled from an isotropic distribution. The vertical dashed line shows the value of $|g_{(II)}|$ above which CS1(II) no longer exists. The bottom panel shows the final equilibrium obliquities (open black circles) for each $g_{(II)}/g_{(I)}$. For the mixed-mode resonances ($g_{\text{res}} \neq 0, \Delta g$), the equilibrium obliquities are given by Eq. (9) and are shown as the solid green and purple lines for the labeled values of g_{res} . The other lines are the equilibrium θ_{eq} for “pure” CSs (as labeled), whose equilibria satisfy Eq. (7). Not all observed mixed-mode resonances are plotted (e.g. for $g_{(II)} = 7.5g_{(I)}$, there is an outcome with $g_{\text{res}}/\Delta g = 3/4$).

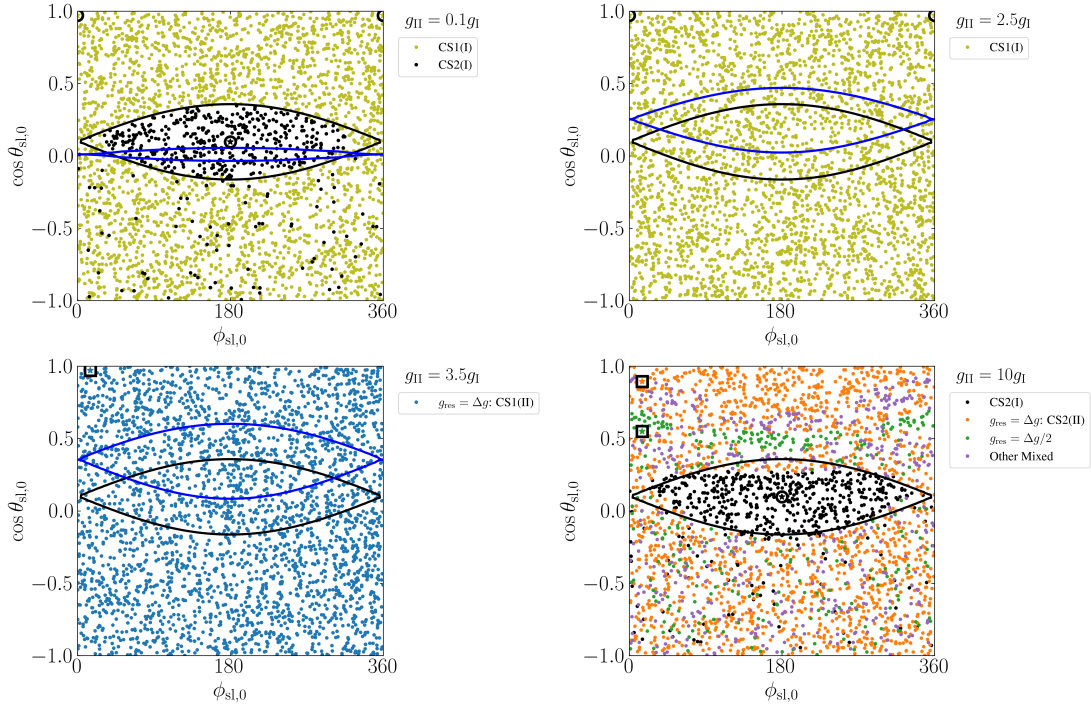


Figure 7: Same as Fig. 3 but for $I_{(II)} = 3^\circ$.

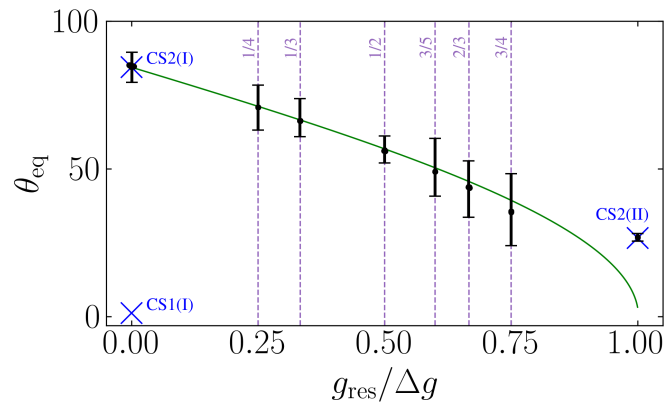


Figure 8: Same as Fig. 5 but for $I_{(II)} = 3^\circ$.

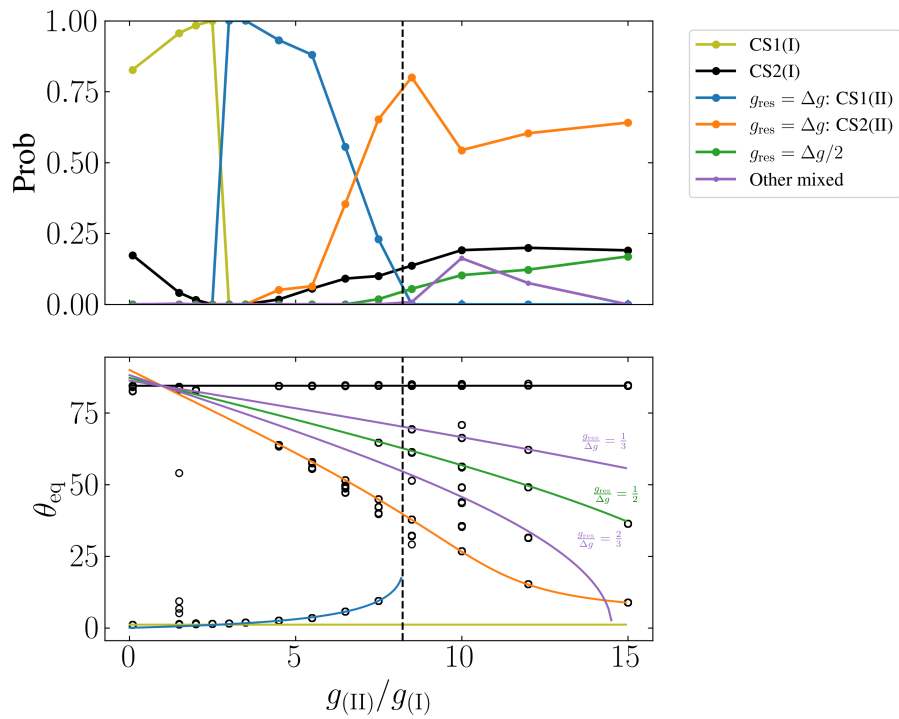


Figure 9: Same as Fig. 6 but for $I_{(II)} = 3^\circ$. Note that the agreement of the black open circles with the theoretical obliquities in the bottom panel is slightly worse than in Fig. 6 but still well within the ranges of oscillation of the obliquities (see Fig. 8 for the characteristic ranges).

Summary of Various Outcomes. In summary, the spin evolution in a 3-planet system driven by a tidal alignment torque depends largely on the frequency of the smaller-amplitude mode, $g_{(\text{II})}$, compared to that of the larger-amplitude mode, $g_{(\text{I})}$. In the regime where $|g_{(\text{I})}| \lesssim \alpha$, we find that:

- When $|g_{(\text{II})}| \ll |g_{(\text{I})}|$, the low-amplitude and slow (II) mode does not significantly affect the spin evolution, and the results of (15) are recovered. The two possible outcomes are the tidally stable CS1(I) (generally low obliquity) and CS2(I) (generally high obliquity). Prograde initial spins converge to CS1(I), spins inside the mode I resonance converge to CS2(I), and retrograde initial spins attain one of these two tidally stable CSs probabilistically.
- When $g_{(\text{II})} \sim g_{(\text{I})}$, CS2(I) is increasingly difficult to attain due to the interacting mode I and mode II resonances, and the probability of attaining CS2(I) can be strongly suppressed (see Fig. 6).
- When $|g_{(\text{II})}| \gtrsim |g_{(\text{I})}|$, there are three classes of outcomes. The highest-obliquity outcome is still CS2(I), and is attained for initial conditions inside the mode I resonance (separatrix; see Fig. 5). The lowest-obliquity outcome is generally CS2(II)³ and is the most favored outcome (see Fig. 6). The third possible outcome are mixed modes with $g_{\text{res}}/\Delta g$ a low-order rational number (see Eq. 8). These mixed modes only appear for $|g_{(\text{II})}| \gg |g_{(\text{I})}|$, and generally have obliquities between those of CS2(I) and CS2(II) (see Fig. 3).

Weak Tidal Friction. We now briefly discuss the spin evolution of the system incorporating the full tidal effects. In the weak friction theory of the equilibrium tide, the spin orientation and frequency jointly evolve following (65–67)

$$\left(\frac{d\hat{\mathbf{S}}}{dt}\right)_{\text{tide}} = \frac{1}{t_s} \left[\frac{2n}{\Omega_s} - (\hat{\mathbf{S}} \cdot \hat{\mathbf{L}}) \right] \hat{\mathbf{S}} \times (\hat{\mathbf{L}} \times \hat{\mathbf{S}}), \quad (10)$$

$$\frac{1}{\Omega_s} \left(\frac{d\Omega_s}{dt}\right)_{\text{tide}} = \frac{1}{t_s} \left[\frac{2n}{\Omega_s} (\hat{\mathbf{S}} \cdot \hat{\mathbf{L}}) - 1 - (\hat{\mathbf{S}} \cdot \hat{\mathbf{L}})^2 \right], \quad (11)$$

where

$$\frac{1}{t_s} \equiv \frac{1}{4k} \frac{3k_2}{Q} \left(\frac{M_\star}{m}\right) \left(\frac{R}{a}\right)^3 n, \quad (12)$$

(see Eq. 1, but with $4k = 1$).

Since $\alpha \propto \Omega_s$ evolves in time, we describe the spin-orbit coupling by the parameter

$$\alpha_{\text{sync}} \equiv [\alpha]_{\Omega_s=n}. \quad (13)$$

To facilitate comparison with the previous results, we use $\alpha_{\text{sync}} = 10 |g_{(\text{I})}|$ and $|g_{(\text{I})}| t_s = 300$. Note that for the physical parameters used in Eqs. (3) and (12), $g_{(\text{I})} t_s \sim 10^4$; we choose a faster tidal timescale to accelerate our numerical integrations. The initial spin is fixed $\Omega_{s,0} = 3n$. We then integrate Eqs. (2), (5), and (10–11) starting from various initial spin orientations and determine the final outcomes. Figure 10 shows the results for a few select values of $g_{(\text{II})}$ and for $I_{(\text{II})} = 3^\circ$. Similar behaviors to Figs. 3 and 7 are

³This may not be the case when $I_{(\text{II})} \lesssim I_{(\text{I})}$ while $g_{(\text{II})} \gg g_{(\text{I})}$; see Fig. A.7 in the Appendix

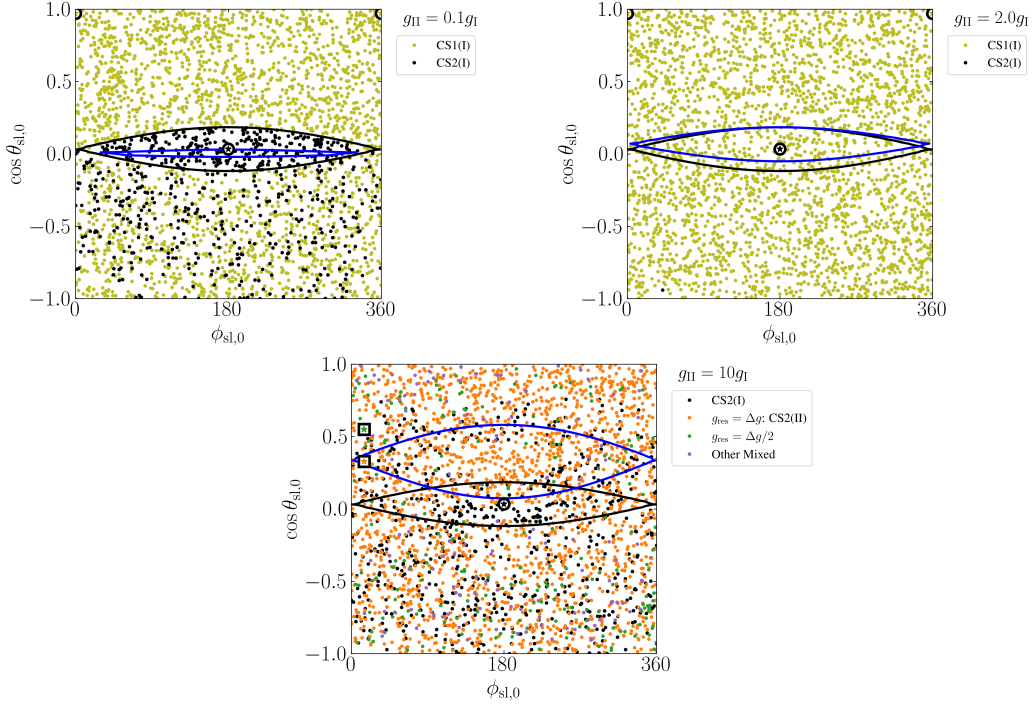


Figure 10: Similar to Figs. 7 but including full tidal effects on the planet’s spin, with $\alpha_{\text{sync}} = 10 |g_{\text{(I)}}|$ (Eq. 13), $I_{\text{(II)}} 3^\circ$, and initial spin $\Omega_{\text{s},0} = 3n$. In the three panels, $g_{\text{(II)}} = \{0.1, 2, 10\} \times g_{\text{(I)}}$ respectively. Note that the plotted separatrices (blue and black lines) use the initial value of α .

observed. The probabilities and obliquities of the various equilibria are shown in Fig. 11. Note that each equilibrium obliquity has a corresponding equilibrium rotation rate, given by

$$\frac{\Omega_{\text{eq}}}{n} = \frac{2 \cos \theta_{\text{eq}}}{1 + \cos^2 \theta_{\text{eq}}}. \quad (14)$$

The probabilities shown in Fig. 11 exhibit qualitative trends that are quite similar to those seen for the evolution driven by the tidal alignment torque alone: when $|g_{\text{(II)}}| \ll |g_{\text{(I)}}|$, the results of (15) are recovered; when $g_{\text{(II)}} \sim g_{\text{(I)}}$, the probability of attaining CS2(I) is significantly suppressed; and when $|g_{\text{(II)}}| \gg |g_{\text{(I)}}|$, mixed modes appear.

Discussion. In this work, we have shown that the planetary spins in compact systems of multiple super-Earths (SEs), possibly with an outer cold Jupiter companion, can be trapped into a number of spin-orbit resonances. In addition to the well-understood tidally-stable Cassini States associated with each of the orbital precession modes, we have also discovered a new class of “mixed mode” spin-orbit resonances that yield substantial obliquities. These additional resonances constitute a significant fraction of the final states of tidal evolution if the planet’s initial spin orientation is broadly distributed, a likely outcome for planets that have experienced an early phase of collisions or giant impacts. A large equilibrium obliquity has a significant influence on the planet’s insolation and climate. For planetary systems surrounding

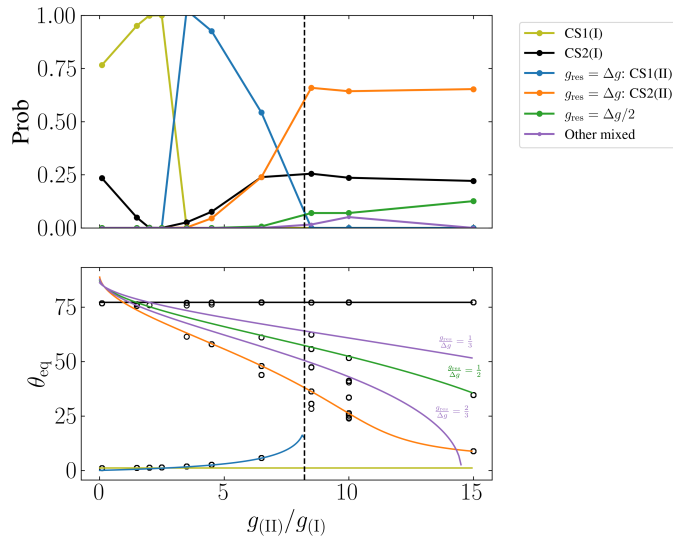


Figure 11: Similar to Fig. 9 but with weak tidal friction.

cooler stars (M dwarfs), the SEs (or Earth-mass planets) studied in this work lie in the habitable zone [e.g. (68, 69)], and the nontrivial obliquity can impact the habitability of such planets.

In a broader sense, the mixed-mode equilibria discovered in our study represent a novel astrophysical example of subharmonic responses in parametrically driven nonlinear oscillators. In equilibrium, the planetary obliquity oscillates with a period that is an integer multiple of the driving period $2\pi/|\Delta g|$ (see Appendix A.2 for discussion). Such subharmonic responses are often seen in nonlinear oscillators [e.g. in the classic van der Pol and Duffing equations, (70–72)]

Throughout this paper, we have adopted fiducial parameters where $|g_{(I)}| \lesssim \alpha$, which is generally expected for the SE systems being studied. If instead $|g_{(I)}| \gtrsim \alpha$, then there is no resonance for the dominant (larger-amplitude) mode I. There are then a few possible cases: if $|g_{(II)}| \lesssim \alpha$, mode II is both slower than mode I and has a smaller amplitude, so it will not affect the mode I dynamics significantly. On the other hand, if $|g_{(II)}| \gtrsim \alpha$, then mode II also has no resonance, and both CS2(I) and CS2(II) have low obliquities, implying that the system will always settle into a low-obliquity state.

Acknowledgements. This work has been supported in part by the NSF grant AST-17152 and NASA grant 80NSSC19K0444. YS is supported by the NASA FINESST grant 19-ASTRO19-0041.

References

1. D. Ferreira, J. Marshall, P. A. O’Gorman, S. Seager, *Icarus* **243**, 236 (2014).
2. A. H. Lobo, S. Bordon, *Icarus* **340**, 113592 (2020).
3. D. S. Spiegel, S. N. Raymond, C. D. Dressing, C. A. Scharf, J. L. Mitchell, *The Astrophysical Journal* **721**, 1308 (2010).

4. J. Armstrong, *et al.*, *Astrobiology* **14**, 277 (2014).
5. M. L. Bryan, *et al.*, *The Astronomical Journal* **159**, 181 (2020).
6. M. L. Bryan, E. Chiang, C. V. Morley, G. N. Mace, B. P. Bowler, *The Astronomical Journal* **162**, 217 (2021).
7. I. A. Snellen, *et al.*, *Nature* **509**, 63 (2014).
8. M. L. Bryan, B. Benneke, H. A. Knutson, K. Batygin, B. P. Bowler, *Nature Astronomy* **2**, 138 (2018).
9. S. Seager, L. Hui, *The Astrophysical Journal* **574**, 1004 (2002).
10. A. D. Adams, S. Millholland, G. P. Laughlin, *The Astronomical Journal* **158**, 108 (2019).
11. K. Ohno, X. Zhang, *The Astrophysical Journal* **874**, 2 (2019).
12. S. Millholland, G. Laughlin, *The Astrophysical Journal Letters* **869**, L15 (2018).
13. S. Millholland, G. Laughlin, *Nature Astronomy* **3**, 424 (2019).
14. S. C. Millholland, C. Spalding, *The Astrophysical Journal* **905**, 71 (2020).
15. Y. Su, D. Lai, *Monthly Notices of the Royal Astronomical Society* **509**, 3301 (2021).
16. S. Tremaine, *Icarus* **89**, 85 (1991).
17. R. M. Jennings, E. Chiang, *Monthly Notices of the Royal Astronomical Society* **507**, 5187 (2021).
18. V. Safronov, E. Zvjagina, *Icarus* **10**, 109 (1969).
19. W. Benz, W. Slattery, A. Cameron, *Meteoritics* **24**, 251 (1989).
20. D. Korycansky, P. Bodenheimer, P. Cassen, J. Pollack, *Icarus* **84**, 528 (1990).
21. L. Dones, S. Tremaine, *Science* **259**, 350 (1993).
22. A. Morbidelli, K. Tsiganis, K. Batygin, A. Crida, R. Gomes, *Icarus* **219**, 737 (2012).
23. J. Li, D. Lai, *The Astrophysical Journal Letters* **898**, L20 (2020).
24. J. Li, D. Lai, K. R. Anderson, B. Pu, *Monthly Notices of the Royal Astronomical Society* **501**, 1621 (2021).
25. Y.-C. Hong, D. Lai, J. I. Lunine, P. D. Nicholson, *The Astrophysical Journal* **920**, 151 (2021).
26. G. Li, *The Astrophysical Journal Letters* **915**, L2 (2021).
27. W. R. Ward, D. P. Hamilton, *The Astronomical Journal* **128**, 2501 (2004).
28. D. P. Hamilton, W. R. Ward, *The Astronomical Journal* **128**, 2510 (2004).
29. W. R. Ward, R. M. Canup, *The Astrophysical Journal Letters* **640**, L91 (2006).

30. D. Vokrouhlický, D. Nesvorný, *The Astrophysical Journal* **806**, 143 (2015).
31. S. Millholland, K. Batygin, *The Astrophysical Journal* **876**, 119 (2019).
32. M. Saillenfest, G. Lari, A. Courtot, *Astronomy & Astrophysics* **640**, A11 (2020).
33. Y. Su, D. Lai, *The Astrophysical Journal* **903**, 7 (2020).
34. M. Saillenfest, G. Lari, G. Boué, *Nature Astronomy* **5**, 345 (2021).
35. Z. Rogozinski, D. P. Hamilton, *The Astrophysical Journal* **888**, 60 (2020).
36. J. Laskar, P. Robutel, *Nature* **361**, 608 (1993).
37. J. Touma, J. Wisdom, *Science* **259**, 1294 (1993).
38. A. C. Correia, J. Laskar, O. N. de Surgy, *Icarus* **163**, 1 (2003).
39. J. J. Lissauer, *et al.*, *The Astrophysical Journal Supplement Series* **197**, 8 (2011).
40. A. W. Howard, *et al.*, *The Astrophysical Journal Supplement Series* **201**, 15 (2012).
41. W. Zhu, C. Petrovich, Y. Wu, S. Dong, J. Xie, *The Astrophysical Journal* **860**, 101 (2018).
42. E. Sandford, D. Kipping, M. Collins, *Monthly Notices of the Royal Astronomical Society* **489**, 3162 (2019).
43. J.-Y. Yang, J.-W. Xie, J.-L. Zhou, *The Astronomical Journal* **159**, 164 (2020).
44. M. Y. He, E. B. Ford, D. Ragozzine, *The Astronomical Journal* **161**, 16 (2021).
45. S. Tremaine, S. Dong, *The Astronomical Journal* **143**, 94 (2012).
46. D. C. Fabrycky, *et al.*, *The Astrophysical Journal* **790**, 146 (2014).
47. M. Y. He, E. B. Ford, D. Ragozzine, D. Carrera, *The Astronomical Journal* **160**, 276 (2020).
48. W. Zhu, Y. Wu, *The Astronomical Journal* **156**, 92 (2018).
49. M. L. Bryan, *et al.*, *The Astronomical Journal* **157**, 52 (2019).
50. K. Masuda, J. N. Winn, H. Kawahara, *The Astronomical Journal* **159**, 38 (2020).
51. S.-F. Liu, Y. Hori, D. Lin, E. Asphaug, *The Astrophysical Journal* **812**, 164 (2015).
52. N. K. Inamdar, H. E. Schlichting, *The Astrophysical Journal Letters* **817**, L13 (2016).
53. A. Izidoro, *et al.*, *Monthly Notices of the Royal Astronomical Society* **470**, 1750 (2017).
54. E. Groten, *Journal of Geodesy* **77**, 724 (2004).
55. V. Lainey, *Celestial Mechanics and Dynamical Astronomy* **126**, 145 (2016).

56. G. Colombo, *The Astronomical Journal* **71**, 891 (1966).
57. S. J. Peale, *The Astronomical Journal* **74**, 483 (1969).
58. S. J. Peale, *The Astronomical Journal* **79**, 722 (1974).
59. W. R. Ward, *The Astronomical Journal* **80**, 64 (1975).
60. J. Henrard, C. Murigande, *Celestial Mechanics* **40**, 345 (1987).
61. D. C. Fabrycky, E. T. Johnson, J. Goodman, *The Astrophysical Journal* **665**, 754 (2007).
62. B. Levrard, *et al.*, *Astronomy & Astrophysics* **462**, L5 (2007).
63. S. Peale, *Extreme Solar Systems* (2008), vol. 398, p. 281.
64. C. D. Murray, S. F. Dermott, *Solar system dynamics* (Cambridge university press, 1999).
65. M. Alexander, *Astrophysics and Space Science* **23**, 459 (1973).
66. P. Hut, *Astronomy and Astrophysics* **99**, 126 (1981).
67. D. Lai, *Monthly Notices of the Royal Astronomical Society* **423**, 486 (2012).
68. C. D. Dressing, *et al.*, *The Astronomical Journal* **154**, 207 (2017).
69. M. Gillon, *et al.*, *Nature* **542**, 456 (2017).
70. M. E. Levenson, *Journal of Applied Physics* **20**, 1045 (1949).
71. J. E. Flaherty, F. Hoppensteadt, *Studies in Applied Mathematics* **58**, 5 (1978).
72. C. Hayashi, *Nonlinear oscillations in physical systems* (Princeton University Press, 2014).
73. B. Pu, D. Lai, *Monthly Notices of the Royal Astronomical Society* **478**, 197 (2018).
74. F. Dai, K. Masuda, J. N. Winn, *The Astrophysical Journal Letters* **864**, L38 (2018).

A Materials and Methods

A.1 Inclination Modes of 3-Planet Systems

In the linear regime, the evolution of the orbital inclinations in a multi-planet system is described by the Laplace-Lagrange theory (64, 73). In this section, we consider 3-planet systems. We denote the magnitude of the angular momentum of each planet by L_j and the inclination relative to the total angular momentum axis $\hat{\mathbf{J}}$ by I_j , and we define the complex inclination $\mathcal{I}_j = I_j \exp[i\Omega_j]$. The evolution equations for \mathcal{I}_1 , \mathcal{I}_2 , and \mathcal{I}_3 are

$$\frac{d}{dt} \begin{pmatrix} \mathcal{I}_1 \\ \mathcal{I}_2 \\ \mathcal{I}_3 \end{pmatrix} = i \begin{pmatrix} -\omega_{12} - \omega_{13} & \omega_{12} & \omega_{13} \\ \omega_{21} & -\omega_{21} - \omega_{23} & \omega_{23} \\ \omega_{31} & \omega_{32} & -\omega_{31} - \omega_{32} \end{pmatrix} \begin{pmatrix} \mathcal{I}_1 \\ \mathcal{I}_2 \\ \mathcal{I}_3 \end{pmatrix}, \quad (15)$$

where ω_{jk} is the precession rate of the j -th planet induced by the k -th planet, and is given by

$$\omega_{jk} = \frac{m_k}{4M_\star} \frac{a_j a_{<}}{a_{>}^2} n_j b_{3/2}^{(1)}(\alpha), \quad (16)$$

where $a_{<} = \min(a_j, a_k)$, $a_{>} = \max(a_j, a_k)$, $n_j = (GM_\star/a_j^3)^{1/2}$, $\alpha = a_{<}/a_{>}$, and

$$b_{3/2}^{(1)}(\alpha) = 3\alpha \left(1 + \frac{15}{8}\alpha^2 + \frac{175}{64}\alpha^4 + \dots \right) \quad (17)$$

is the Laplace coefficient. Eq. (15) can be solved in general, giving two non-trivial eigenmodes. In the limit $L_1 \ll L_2, L_3$, the two eigenmodes have simple solutions and interpretations:

- Mode I has frequency

$$g_{(\text{I})} = -(\omega_{12} + \omega_{13}). \quad (18)$$

It corresponds to free precession of $\hat{\mathbf{L}}_1$ around the total angular momentum $\mathbf{J} = \mathbf{L}_2 + \mathbf{L}_3$. The amplitude of oscillation of $\hat{\mathbf{L}}_1$, $I_{(\text{I})}$, is simply the inclination of $\hat{\mathbf{L}}_1$ with respect to $\hat{\mathbf{J}}$.

- Mode II has frequency

$$g_{(\text{II})} = -(\omega_{23} + \omega_{32}) = -\frac{J}{L_3}\omega_{23}, \quad (19)$$

which is simply the precession frequency of $\hat{\mathbf{L}}_2$ (or $\hat{\mathbf{L}}_3$) about $\hat{\mathbf{J}}$. The forced oscillation of $\hat{\mathbf{L}}_1$ has an amplitude

$$I_{(\text{II})} = \frac{\omega_{12}L_3 - \omega_{13}L_2}{(g_{(\text{II})} - g_{(\text{I})})J} I_{23}, \quad (20)$$

where I_{23} is the mutual inclination between the two outer planets and is constant.

We consider two archetypal 3-planet configurations, systems with three super Earths (SEs) and systems with two inner SEs and an exterior cold Jupiter (CJ). In both cases, we take the inner two planets to have $m_1 = M_\oplus$, $m_2 = 3M_\oplus$, $a_1 = 0.1$ AU, and we consider three values of $a_2 = \{0.15, 0.2, 0.25\}$ AU. For the 3SE case, we take $m_3 = 3M_\oplus$ and the characteristic inclinations $I_1 \simeq I_{23} \simeq 2^\circ$ [corresponding to three nearly-coplanar SEs; see (46, 74)]. For the 2SE + CJ case, we take $m_3 = 0.5M_J$ and the characteristic inclinations $I_1 \simeq I_{23} \simeq 10^\circ$ [corresponding to a mildly inclined CJ; see (50)]. In both cases, we compute the mode precession frequencies $g_{(\text{I,II})}$ and characteristic mode amplitudes $I_{(\text{I,II})}$ for a range of a_3 . Figures A.1–A.3 show examples of our results.

A.2 Additional Comments and Results on Mixed Mode Equilibria

In the main text, we provided an example of the spin evolution into a mixed-mode equilibrium in Fig. 2 for the parameters $I_{(\text{I})} = 10^\circ$, $I_{(\text{II})} = 1^\circ$, $\alpha = 10|g_{(\text{I})}|$, and $g_{(\text{II})} = 10g_{(\text{I})}$. In Fig. A.4, we provide several further examples of the evolution into other mixed-mode equilibria with different values of g_{res} when $I_{(\text{II})} = 3^\circ$ is used. We find that their average equilibrium obliquities θ_{eq} are still well-described by Eq. (9). Furthermore, we find that, if $g_{\text{res}}/\Delta g = p/q$ for integers p and q , then the steady-state oscillations of θ_{sl} are periodic with period $2\pi q/|\Delta g|$ (see bottom example in Fig. 2 for the case of $g_{\text{res}} = \Delta g/2$).

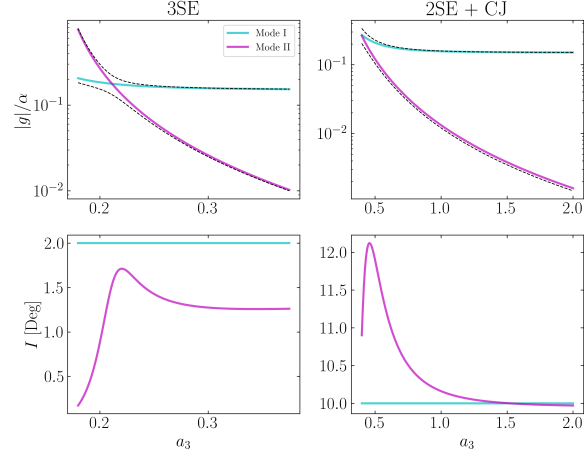


Figure A.1: Inclination mode frequencies and amplitudes for the 3SE (left) and 2SE + CJ (right) systems. In both systems, the inner planets' parameters are $m_1 = M_\oplus$, $m_2 = 3M_\oplus$, $a_1 = 0.1$ AU, $a_2 = 0.15$ AU. In the 3SE case, $m_3 = 3M_\oplus$ and $I_1 = I_{23} = 2^\circ$, while in the 2SE + CJ case, $m_3 = 0.5M_J$ and $I_1 = I_{23} = 10^\circ$. In the top panels, the black dashed lines show the mode frequencies from the exact solution of Eq. (15), while the solid, colored lines are given by Eqs. (18, 19).

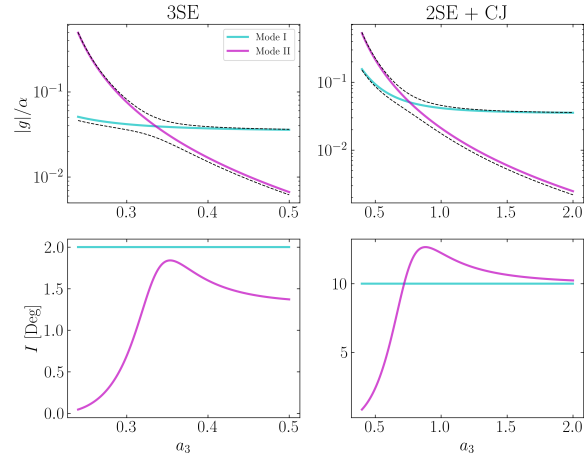


Figure A.2: Same as Fig. A.1 but for $a_2 = 0.2$ AU.

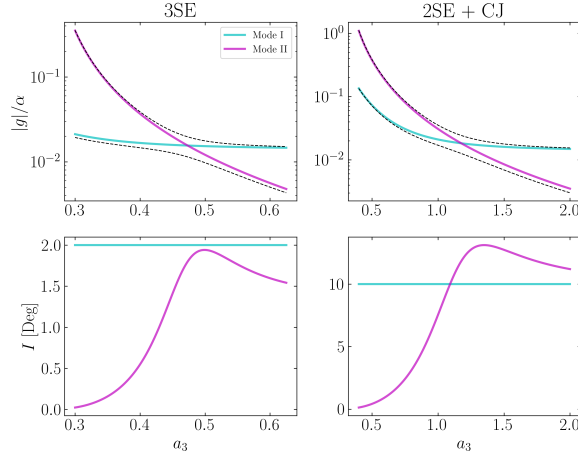


Figure A.3: Same as Fig. A.1 but for $a_2 = 0.25$ AU.

Figure A.5 shows the equilibrium obliquity θ_{eq} as a function of g_{res} for a system with $I_{(\text{II})} = 3^\circ$ and $g_{(\text{II})} = 8.5g_{(\text{I})}$. We can see for $g_{\text{res}} = \Delta g$ that there are three distinct equilibrium values of θ_{sl} . The largest-obliquity equilibrium is CS2(II), and the equilibrium with an intermediate obliquity is a mixed-mode equilibrium with $g_{\text{res}} = \Delta g$, as it directly intersects the green line (Eq. 9). The existence and stability of this equilibrium is responsible for the extra dot a few degrees below the CS2(II) curve in the bottom panels of Figs. 6, 9, and 11 (e.g. most visible for $g_{(\text{II})}/g_{(\text{I})} = 6.5, 7.5,$ and 8.5 in Fig. 9). The origin of the lowest-obliquity equilibrium at $g_{\text{res}} = \Delta g$ in Fig. A.5 is distinct, though it is within the range of oscillation of θ_{sl} of the mixed-mode steady state.

In Fig. 4, we presented the numerical stability analysis of initial conditions in the neighborhood of the mixed-mode equilibrium for the $I_{(\text{II})} = 1^\circ$ case. When $I_{(\text{II})}$ is increased to 3° , the amplitudes of oscillations of the mixed-mode equilibria begin to overlap (see Fig. 8), and so we might expect that the basins of attraction for the resonances overlap in $\theta_{\text{sl},0}$ space. Figure A.6 shows that this is indeed the case, and that the basins of attraction of the mixed modes are very distorted (likely due to interactions among the resonances) compared to those seen in the $I_{(\text{II})} = 1^\circ$ case.

Finally, in the main text, we have focused on the regime where $I_{(\text{II})} \ll I_{(\text{I})}$. In Fig. A.7, we show the effect of choosing $I_{(\text{II})} = 9^\circ$ (with the same that $I_{(\text{I})} = 10^\circ$). It can be seen that the $g_{\text{res}} = \Delta g/2$ mixed mode is the most common outcome when $|g_{(\text{II})}| \gg |g_{(\text{I})}|$, as it is the preferred low-obliquity equilibrium ($\theta_{\text{eq}} \lesssim 20^\circ$) for $g_{(\text{II})} = 15g_{(\text{I})}$. The degraded agreement of the θ_{eq} values with Eq. (9) is because our theoretical results assume $I_{(\text{II})} \ll I_{(\text{I})}$. A broad range of final obliquities is observed when $g_{(\text{II})} = 6.5g_{(\text{I})}$, very close to the critical value of $g_{(\text{II})}$ (denoted by the vertical dashed line) where the number of mode II CSs changes from 4 to 2 (15). This is likely due to the unusual phase space structure near this bifurcation.

A.3 Analytical Derivation of Mixed-Mode Obliquities

The objective of this section is to derive Eq. (9), which relates g_{res} of a mixed-mode equilibrium to the average obliquity θ_{eq} in the equilibrium. We consider the equation of motion in the rotating frame where

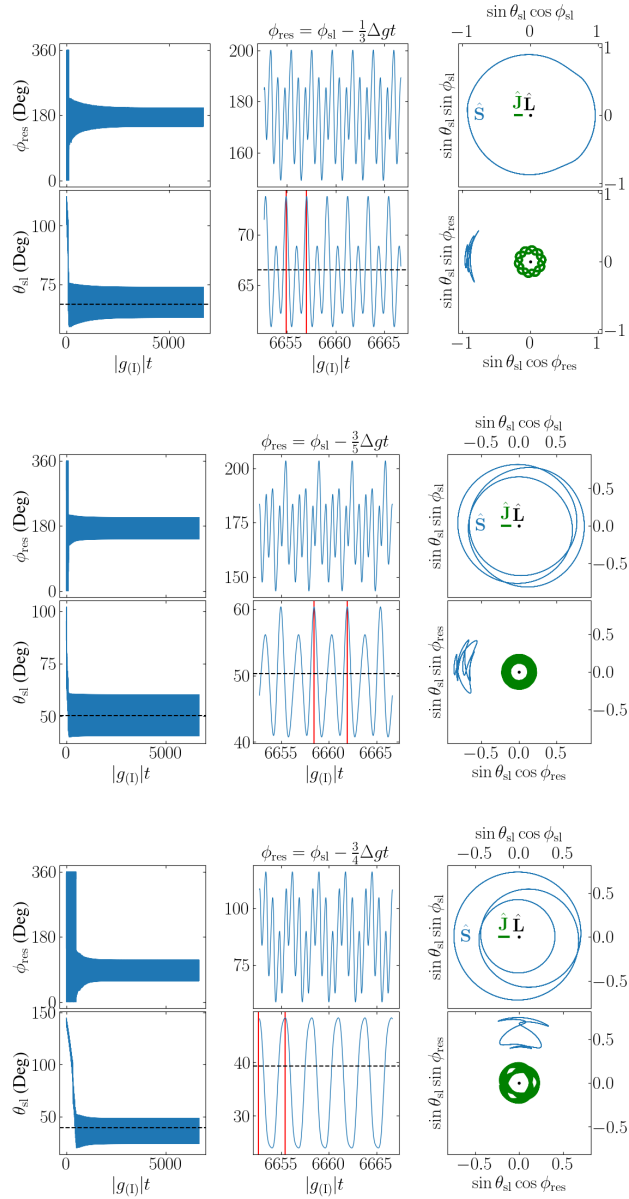


Figure A.4: Same as Fig. 2 but for $\overline{g}_{(\text{II})} = 10\overline{g}_{(\text{I})}$ and $I_{(\text{II})} = 3^\circ$. The three examples correspond to capture into mixed-mode equilibria with resonant angles corresponding to $g_{\text{res}} = \Delta g/3$, $g_{\text{res}} = 3\Delta g/5$, and $g_{\text{res}} = 3\Delta g/4$ respectively. The three pairs of vertical red lines are separated by $6\pi/|\Delta g|$, $10\pi/|\Delta g|$, and $8\pi/\Delta g$ in the three examples respectively.

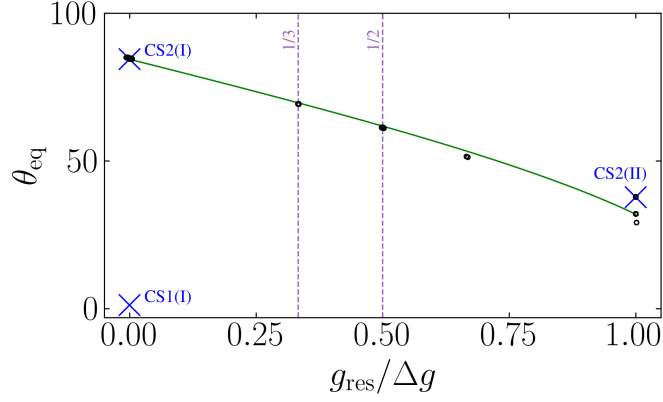


Figure A.5: Same as Figs. 5 and 8 but for $I_{(II)} = 3^\circ$ and $g_{(II)} = 8.5g_{(I)}$, where ranges of oscillation in θ_{sl} have been suppressed for clarity.

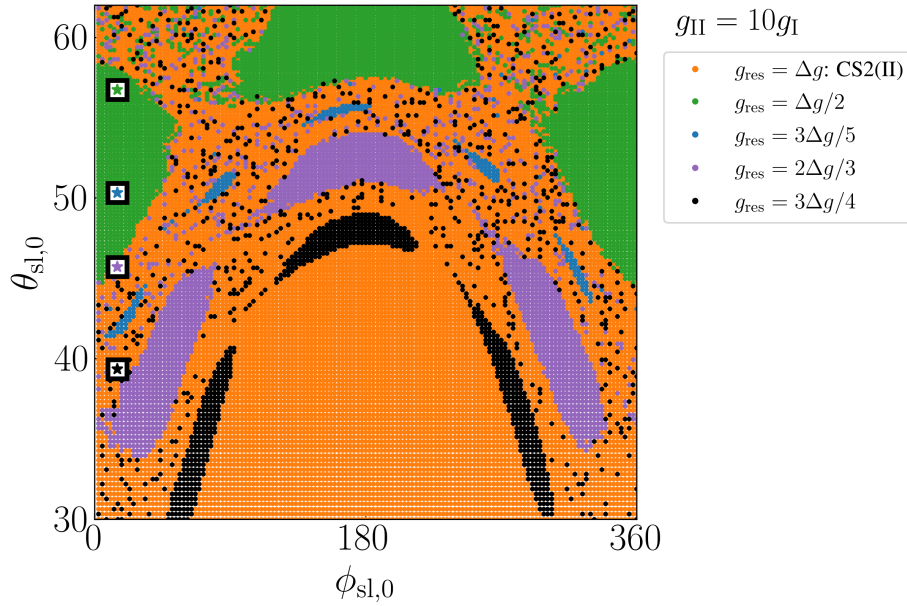


Figure A.6: Same as Fig. 4 but for $I_{(II)} = 3^\circ$. The range of the vertical axis is chosen to include the ranges of oscillation of the $1/2$, $3/5$, $2/3$, and $3/4$ mixed mode resonances (see Fig. 8). The decreasing density of points as $\theta_{sl,0}$ decreases is because the grid of initial conditions is uniform in $\cos \theta_{sl,0}$ rather than $\theta_{sl,0}$ itself.

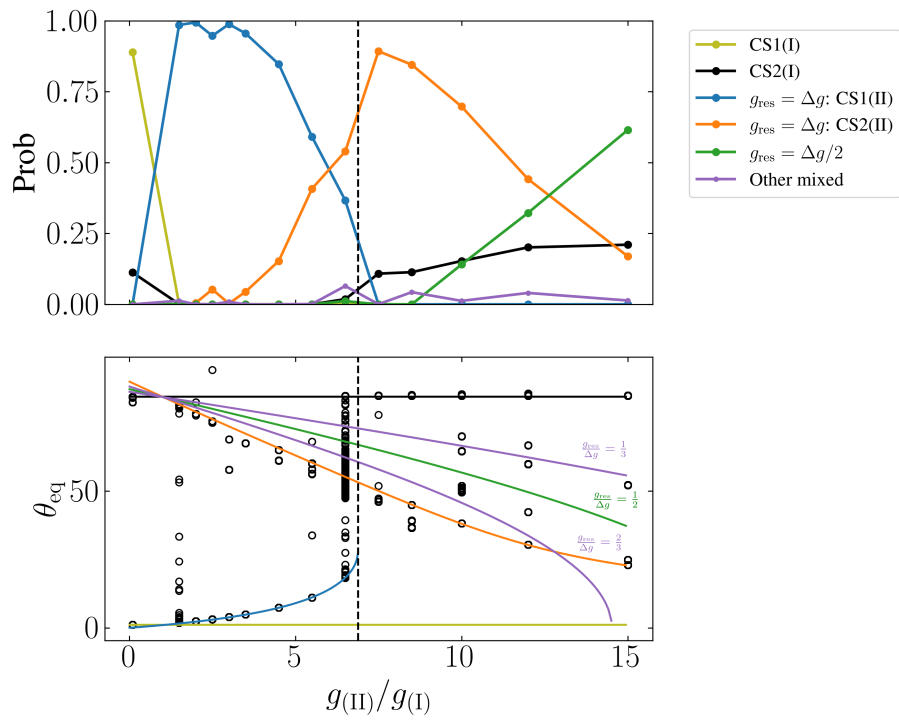


Figure A.7: Same as Fig. 6 but for $I_{(II)} = 9^\circ$.

$\hat{\mathbf{L}} = \hat{\mathbf{z}}$ is constant and $\hat{\mathbf{J}}$ lies in the xz plane (i.e. $\hat{\mathbf{J}} = -\sin I \hat{\mathbf{x}} + \cos I \hat{\mathbf{z}}$):

$$\left(\frac{d\hat{\mathbf{S}}}{dt} \right)_{\text{rot}} = \alpha (\hat{\mathbf{S}} \cdot \hat{\mathbf{L}}) (\hat{\mathbf{S}} \times \hat{\mathbf{L}}) + \hat{\mathbf{S}} \times (\dot{\Omega} \hat{\mathbf{J}} + \dot{I} \hat{\mathbf{y}}). \quad (21)$$

Let $\hat{\mathbf{S}} = \sin \theta_{\text{sl}} (\cos \phi_{\text{sl}} \hat{\mathbf{x}} + \sin \phi_{\text{sl}} \hat{\mathbf{y}}) + \cos \theta_{\text{sl}} \hat{\mathbf{z}}$. The evolution of ϕ_{sl} then follows

$$\begin{aligned} \frac{d\phi_{\text{sl}}}{dt} = & -\alpha \cos \theta_{\text{sl}} - \dot{\Omega} (\cos I + \sin I \cot \theta_{\text{sl}} \cos \phi_{\text{sl}}) \\ & - \dot{I} \cot \theta_{\text{sl}} \sin \phi_{\text{sl}}. \end{aligned} \quad (22)$$

Note that the single-mode CSs satisfy Eq. (22) where $\dot{\Omega} = g$, $\dot{I} = 0$, and ϕ_{sl} is either equal to 0° or 180° (Eq. 7). For the general, two-mode problem, if $\phi_{\text{res}} = \phi_{\text{sl}} - g_{\text{res}} t$ is a resonant angle, then it must satisfy

$$\left\langle \frac{d\phi_{\text{res}}}{dt} \right\rangle = \left\langle \frac{d\phi_{\text{sl}}}{dt} \right\rangle - g_{\text{res}} = 0, \quad (23)$$

where the angle brackets denote an average over a libration period. Since ϕ_{sl} circulates when $g_{\text{res}} \neq 0$, $\langle \cos \phi_{\text{sl}} \rangle = \langle \sin \phi_{\text{sl}} \rangle = 0$. Furthermore, if $I_{(\text{II})}/I_{(\text{I})} \equiv \epsilon \ll 1$, we can expand Eq. (4) to obtain

$$\dot{\Omega} = g_{(\text{I})} + \Delta g \epsilon \cos(\Delta g t) + \mathcal{O}[\epsilon^2], \quad (24)$$

$$I = I_{(\text{I})} (1 + \epsilon \cos(\Delta g t) + \mathcal{O}[\epsilon^2]), \quad (25)$$

where $\Delta g \equiv g_{(\text{II})} - g_{(\text{I})}$. To leading order, we have $\dot{\Omega} \simeq g_{(\text{I})}$ and $I \simeq I_{(\text{I})}$, so Eq. (22) reduces to

$$\alpha \cos \theta_{\text{eq}} \simeq -g_{(\text{I})} \cos I_{(\text{I})} - g_{\text{res}}. \quad (26)$$

This is Eq. (9) in the main text, and is shown in Fig. 5. Good agreement between the analytic expression and numerical results is observed. Note that setting $g_{\text{res}} = \Delta g$ in Eq. (9) does not yield the mode II CSs, as the mode I inclination is still being used, and the ϕ_{sl} terms are averaged out in the mixed mode calculation while being nonzero in the CS obliquity calculation.